



1 **Aggregation of Slightly Buoyant Microplastics in Three-Dimensional Vortex Flows**

2 Irina I. Rypina¹, Larry J. Pratt¹, and Michael Dotzel¹

3 ¹ Woods Hole Oceanographic Institution, Physical Oceanography Department, 266 Woods Hole
4 Rd., Woods Hole, MA 02543

5 Corresponding author email: irypina@whoi.edu

6

7

8

9

10

11

12

13

14

15

16

17

18



19 **Abstract**

20 Although the movement and aggregation of microplastics at the ocean surface has been well
21 studied, less is known about the subsurface. Within the Maxey-Riley framework governing the
22 movement of small spheres with high drag in fluid, aggregation of buoyant particles is
23 encouraged in vorticity-dominated regions. We explore this process in an idealized model of a
24 three-dimensional eddy with an azimuthal and overturning circulation. In the axially symmetric
25 state, particles that do not accumulate at the top boundary are attracted to a closed contour
26 consisting of periodic orbits. Such a contour exists when drag on the particle is sufficiently
27 strong. For small slightly-buoyant particles, this contour is located close to the periodic fluid
28 trajectory. If the symmetric flow is perturbed by a symmetry-breaking disturbance, additional
29 attractors arise near periodic orbits of fluid particles within the resonance zones created by the
30 disturbance. Disturbances with periodic time dependence produce even more attractors, with a
31 shape and location that recurs periodically, and which are composed of quasiperiodic orbits of
32 rigid particles. Not all such contours attract, and particles released in the vicinity may instead be
33 attracted to a nearby attractor. Examples are presented along with mappings of the respective
34 basins of attraction.

35

36

37

38

39



40 **Significance statement**

41 This paper investigates the phenomenon of aggregation of small, slightly buoyant, rigid body
42 particles in a three-dimensional vortex flow. Our goal was to gain insights into the behaviour of
43 slightly buoyant marine microplastic particles in a flow that qualitatively resembles ocean
44 eddies. Attractors are mapped out for the steady axisymmetric, steady asymmetric, and non-
45 steady asymmetric vortices over a range of flow and particle parameters. Simple theoretical
46 arguments are used to interpret the results.

47

48

49

50

51

52

53

54

55

56

57



58 I. Introduction

59 Marine microplastic pollution has been a rising concern for the ocean environmental and for
60 human health. Microplastics (scales < 5mm) and nanoplastics (scales < 1 μm) have been found
61 in the tissues of marine animals, some of which are consumed by humans (Landrigan, et al.
62 2023). This comes at a time when global production of plastics is projected to increase. Most
63 observations of marine microplastics have occurred at or near the sea surface, where
64 concentrations are largest. However, the density of many types of particles, including high-
65 density polyethylene, is sufficiently close to that of sea water that suspension within the water
66 column for long periods of time is feasible. Indeed, microplastics have been found well beneath
67 the ocean surface, but less is known regarding their spatio-temporal distributions (Shamskhany et
68 al. 2021).

69 A potentially important aspect of the movement of plastics and microplastics is aggregation, a
70 process that occurs at the surface over large scales near the centers of the five major subtropical
71 gyres and has been attributed to Ekman drift, windage and inertia (Beron-Vera, 2021). Many
72 early models concentrated on the ocean surface, but Froyland et al. (2014) has highlighted the
73 importance of resolving the full three dimensional circulation. If aggregation also occurs below
74 the surface, well beneath the direct influence of Ekman layers, the dynamics is likely to be
75 different. Indeed, modeling results by Wichmann et al. (2019), and based on a framework
76 created by Lange and van Sebille (2017) and Delandmeter and van Sebille (2019), suggests that
77 the large scale accumulation associated with the garbage patches disappears below 60m depth.
78 Typically the position $X(t)$ of a non-fluid particle is tracked according to

$$79 \quad X(t + \Delta t) = X(t) + \int_t^{t+\Delta t} v dt + dX_b,$$



80 where v is the fluid velocity and dX_b is an extra displacement due the non-fluid nature of the
81 particle. The user can introduce custom schemes for calculating contributions to dX_b due to
82 factors such as windage and inertia (e.g. Beron-Vera et al. 2016), turbulent diffusion (e.g.
83 Kulkulka, 2012), wave induced Stokes drift (Onink et al. 2019), etc. Eulerian schemes in which
84 plastic particles are treated as concentrations, are rare, but Mountford and Morales Maqueda
85 (2019) developed an Eulerian model in which concentrations are advected by the fluid and are
86 subject to parameterized turbulence as well as sinking or rising according to a simple law
87 involving buoyancy and friction.

88 An alternative approach would be to use the Maxey-Riley equation (discussed below) to solve
89 for the particle velocity v in the above equation, then use the latter to compute the trajectory of
90 that parcel. This equation would account for effects such as inertia and added mass in a
91 deductive way, however the resulting 6th-order system (for the three components of velocity and
92 position) would be computationally challenging. To better understand the implications of the use
93 of this approach while avoiding the computational burden and complexity, we have elected to
94 analyze the movement and aggregation of individual particles using a Maxey-Riley framework in
95 connection with an idealized, 3D flow field resembling the circulation in an ocean eddy. The aim
96 is to develop a basic understanding of the circumstances that would lead to aggregation of rigid
97 particles in ocean mesoscale and submesoscale eddies. We note that other idealized studies have
98 been carried out in connection with 2D wave fields and vortex flows (e.g. DiBenedetto 2018a,b
99 and Kelly et al., 2021).

100 Aggregation can be attributed to the presence of an attractor: here, an object with a dimension
101 less than three that is somehow set up by the fluid circulation patterns and towards which rigid
102 particle trajectories attract. As long as the fluid is incompressible, fluid parcels will not



103 experience attraction and will not aggregate, but plastic particles with inertia, added mass, and
104 drag may do so. In order to reach a better understanding of what leads to attraction and attractors
105 in 3D flows, we explore a canonical example in geophysical fluid dynamics, namely the flow in
106 a rotating cylinder. This flow has some of the characteristics of ocean eddies, including a
107 horizontal swirl and an overturning component in the vertical. The Lagrangian properties of this
108 circulation have been previously studied (Fountain, et al. 2000; Pratt et al. 2014; Rypina et al.
109 2015) allowing us to begin to investigate inertial particles from an established base of
110 knowledge. A prior theory (Haller and Sapsis, 2008) governing the movement of particles with
111 high drag indicates that accumulation is favored for slightly buoyant particles in flows dominated
112 by vorticity, and this also motivates our choice of background flow. Identification of the
113 attractors that can arise in this flow field, evaluating their reach and domains of attraction, and
114 clarifying the circumstances that lead to their formation are the primary objectives of this work.

115 II. Methods

116 The physics of the motion of a small, rigid sphere that moves with velocity $\vec{v}(t)$ through a fluid
117 with pre-existing velocity distribution $\vec{u}(\vec{x}, t)$ has been the subject of investigation by Stokes
118 (1851), Basset (1888), Boussinesq (1903), Faxen (1922), Oseen (1927), Tchen (1947) and many
119 others, and was put in a unifying framework by Maxey and Riley (1983). More recent
120 theoretical extensions include Beron-Vera et al. (2019) and Beron-Vera (2021). We will use a
121 form of the Maxey-Riley equation that has been extended to include constant frame rotation with
122 angular velocity $\vec{\Omega}^*$:

$$123 \quad \frac{d\vec{v}}{dt} = \frac{\rho_f}{\rho_p} \frac{D\vec{u}}{Dt} + \frac{\rho_f}{2\rho_p} \left(\frac{D\vec{u}}{Dt} - \frac{d\vec{v}}{dt} \right) - \frac{9\nu\rho_f}{2\rho_p d^2} (\vec{v} - \vec{u}) + \left(1 - \frac{\rho_f}{\rho_p} \right) \vec{g} + \frac{\rho_f}{\rho_p} \vec{\Omega}^* \times (\vec{u} - \vec{v})$$



124
$$+ \frac{\rho_f}{\rho_p} 2\vec{\Omega}^* \times \vec{u} - 2\vec{\Omega}^* \times \vec{v} + \left(\frac{\rho_f}{\rho_p} - 1 \right) \vec{\Omega}^* \times \vec{\Omega}^* \times r. \quad (1)$$

125 In this statement of Newton's second law for the rigid particle, the right-hand side represents, in
126 order, the effects of inertia, added mass, drag, buoyancy, Coriolis acceleration associated with
127 the added mass, the Coriolis acceleration associated with the particle mass, Coriolis acceleration
128 associated with the fluid motion, and centripetal acceleration. (See Beron-Vera, et al. 2019 for a
129 derivation, though the centripetal acceleration appears to have been omitted.) We have omitted
130 the lift force, the Basset history force, and the Faxen corrections (Gatignol, 1983). Here ρ_p and
131 ρ_f are densities of the particle and the fluid, d is the particle radius, ν is viscosity of the fluid, \vec{g}
132 is the gravity vector, and $\frac{D\vec{u}}{Dt} = \frac{\partial\vec{u}}{\partial t} + \vec{u} \cdot \nabla\vec{u}$ is the fluid material derivative, evaluated for
133 undisturbed fluid velocity at the position of the center of the particle. The position $x_p(t)$ of a
134 particle is determined by

135
$$\frac{dx_p}{dt} = \vec{v}, \quad (2)$$

136 and together (1) and (2) compose a coupled, 6th-order system for computation of the particle
137 position and velocity as functions of time.

138 If the velocities and lengths are nondimensionalized using characteristic scales U and L for the
139 background fluid flow, and L/U is used as a time scale, then (2) remains formally unchanged
140 while the nondimensional form of (1) is

141
$$\frac{d\vec{v}}{dt} = \frac{3R}{2} \frac{D\vec{u}}{Dt} + \varepsilon^{-1}(\vec{v} - \vec{u}) + \left(1 - \frac{3R}{2}\right) \vec{g}_r + 3R\vec{\Omega} \times (\vec{u} - \vec{v}) + 2\left(\frac{3R}{2} - 1\right) \vec{\Omega} \times \vec{v}, \quad (3)$$



142 where $R = \frac{2\rho_f}{\rho_f + 2\rho_p}$, $\vec{g}_r = (\vec{g} - \vec{\Omega}^* \times \vec{\Omega}^* \times \vec{r}) / (\frac{U^2}{L})$, $\vec{\Omega} = \frac{\vec{\Omega}^* L}{U}$ and $\tilde{\varepsilon} = \frac{2}{9} \left(\frac{d}{L}\right)^2 \frac{UL}{\nu R}$ is the Stokes
143 number, the ratio of the adjustment time scale of a particle (due to drag) to the time scale of the
144 background flow. For $\tilde{\varepsilon} \ll 1$, viscous drag is the dominant force acting on the particle, implying
145 that a particle with an initial velocity differing by an amount $> O(\tilde{\varepsilon})$ from the local fluid velocity
146 will be rapidly accelerated over a time scale $\tilde{\varepsilon}$ to a velocity proximal to that of the fluid.
147 Thereafter the particle will undergo a slow evolution in which the weaker forces due to inertia,
148 added mass, and buoyancy cause slight departures from the movement of the fluid itself.

149 The limit $\tilde{\varepsilon} \rightarrow 0$ constitutes a singular perturbation of (3), a problem that can be addressed using
150 an approach due to Fenichel (1979) that was originally formally developed for a steady
151 background flow, but that has been extended by Haller and Sapsis (2008) to include a time-
152 varying background flow. In either case, it can be shown that following the initial viscous
153 adjustment, the particle position and velocity tend toward a subspace or “slow manifold” on
154 which the particle velocity is determined directly by the fluid velocity through an “inertial”
155 equation, here extended to include frame rotation:

$$156 \quad \vec{v} = \vec{u} + \tilde{\varepsilon} \left(\frac{3R}{2} - 1 \right) \left[\frac{D\vec{u}}{Dt} + 2\vec{\Omega} \times \vec{u} - \vec{g}_r \right] + O(\tilde{\varepsilon}^2). \quad (4)$$

157 This version with rotation was written down in Beron-Vera et al. 2019, though with \vec{g}_r replaced
158 by the non-generalized gravity vector \vec{g} . The same authors also present more general cases,
159 including those with the lift force. In Supplementary Material we present a simple, alternative
160 derivation of Eq. (4) based on a multiple-scale expansion instead of the Fennochel approach.

161 A chief advantage of the slow manifold reduction is that the 6th order system (2) and (3) is
162 reduced to a 3rd order system (2) and (4) in which the particle velocity is known in advance.



163 The bracketed expression in (4), which determines the velocity of the rigid particle relative to the
164 fluid, is nothing more than $\frac{\partial}{\partial x_j} \tau_{ij}$, where τ_{ij} is the stress tensor for the fluid. Thus the relative
165 velocity of a rigid particle on the slow manifold is in the same direction as the net force that
166 would act on a fluid particle occupying the same space. Ordinarily, for a fluid particle, that force
167 would equate with an acceleration, but on the slow time scale, the relative particle velocity points
168 in the same direction as the net fluid force and its magnitude is proportional to $\tilde{\varepsilon} \left(\frac{3R}{2} - 1 \right)$
169 $= \frac{2}{9} \frac{d^2}{L^2} \frac{UL}{\nu} \frac{(\rho_f - \rho_p)}{\rho_f}$. Since the aggregation of rigid particles requires departures of the particle
170 velocity from the (divergence free) velocity field of the fluid, one can expect that aggregation
171 will occur more slowly if d and $(\rho_f - \rho_p)/\rho_f$ are small, or if ν is large. At the same time, the
172 existence of attractors internal to the fluid may depend on $(\rho_f - \rho_p)/\rho_f$ being small: for
173 example, a large density difference may mean that rigid particles simply sink to the bottom or
174 rise to the surface.

175 As pointed out by Haller and Sapsis (2008) (also see Beron-Vera et al. 2019), we can consider a
176 continuous concentration of rigid particles with the like properties, and with smoothly varying
177 velocity (4). The aggregation of such a concentration would appear to require that the
178 divergence of that velocity be negative (though see an apparent counterexample, presented later).
179 Following Haller and Sapsis (2008), consider the evolution of a material volume of rigid
180 particles. The time rate of change of this volume is

$$181 \quad \frac{dV}{dt} = \oint \vec{v} \cdot \vec{n} dA_V = \iiint (\nabla \cdot \vec{v}) dV = \iiint \nabla \cdot \left[\vec{u} + \tilde{\varepsilon} \left(\frac{3R}{2} - 1 \right) \left(\frac{D\vec{u}}{Dt} + 2\vec{\Omega} \times \vec{u} - \vec{g}_r \right) \right] dV \quad (5)$$



182 where $\nabla \cdot \vec{u} = 0$ for an incompressible fluid. Shrinking V to an infinitesimal size allows the right-
 183 hand side to be approximated by V times the local value in the integrand, and the result may be
 184 integrated in time, yielding

$$\begin{aligned}
 185 \quad V(t) &= V_0 \exp \left(\tilde{\varepsilon} \left(\frac{3R}{2} - 1 \right) \int_{t_0}^t \nabla \cdot \left(\frac{D\vec{u}}{Dt} + 2\vec{\Omega} \times \vec{u} - \vec{g}_r \right) ds \right) \\
 186 \quad &= V_0 \exp \left(-2\tilde{\varepsilon} \left(\frac{3R}{2} - 1 \right) \int_{t_0}^t [Q_r(x(s), s) + \vec{\Omega} \cdot \vec{\zeta}_r + |\vec{\Omega}|^2] ds \right) \\
 187 \quad &= V_0 \exp \left(-2\tilde{\varepsilon} \left(\frac{3R}{2} - 1 \right) \int_{t_0}^t Q_a(x(s), s) ds \right). \tag{6}
 \end{aligned}$$

188 Here $Q_r = \frac{1}{2} \left(|\vec{\zeta}_r|^2 - |S|^2 \right)$ is the three-dimensional Okubo-Weiss parameter (Okubo, 1970;
 189 Weiss, 1991), $\vec{\zeta}_r$ represents the relative vorticity vector for the fluid, $S = 1/2(\nabla\vec{u} + (\nabla\vec{u})^T)$ is
 190 the strain tensor, and $|S|$ is its Frobenius norm. The final step in (6) follows from introduction of
 191 the absolute vorticity vector

$$192 \quad \vec{\zeta}_a = \vec{\zeta}_r + 2\vec{\Omega} \tag{7}$$

193 and the corresponding function $Q_a = \frac{1}{2} \left(|\vec{\zeta}_a|^2 - |S|^2 \right)$. We note that for a volume V of any size:

$$\begin{aligned}
 194 \quad \frac{dV}{dt} &= 2\tilde{\varepsilon} \left(\frac{3R}{2} - 1 \right) \iiint Q_a dV = \tilde{\varepsilon} \left(\frac{3R}{2} - 1 \right) \iiint \frac{\partial^2}{\partial x_i \partial x_j} \tau_{ij} dV = \frac{2}{9} \frac{d^2}{L^2} \frac{UL}{\nu} \frac{(\rho_f - \rho_p)}{\rho_f} \oint \frac{\partial}{\partial x_j} \tau_{ij} n_i dA_V, \\
 195 \quad &\tag{8}
 \end{aligned}$$

196 where n_j denote the components of the outward unit vector normal to the bounding surface A_V .
 197 Thus for buoyant particles, a volume $V(t)$ of any size will contract if the force normal to A_V due
 198 to the fluid stresses, integrated around A_V , is inward. In many cases the stress tensor is



199 dominated by pressure, i.e., $\frac{\partial}{\partial x_j} \tau_{ij} \cong -\frac{1}{\rho_f} \nabla p$, so the tendency to aggregate is determined entirely
200 by the pressure field.

201 In general, Q_a can change sign along a particle trajectory, making it hard to predict whether the
202 surrounding volume shrinks or expands with time. If a buoyant particle is trapped in a region in
203 which Q_a is predominately positive, then this region is a good candidate for aggregation.
204 Persistent ocean eddies and other vortical structures are possibilities, not only because vorticity
205 tends to dominate over strain, but also because such features have the ability to trap fluid for long
206 periods of time. For dense particles, contraction occurs in areas dominated by strain, and it has
207 been shown that aggregation of heavy particles can occur in strain-dominated filaments that arise
208 in particle-laden turbulent flows, though the considered particle-to-fluid density differences tend
209 to be quite large (see Brandt and Coletti, 2022 for a review). In our study, we will focus on
210 eddies, and on lower dimension objects within eddies that can act as attractors for buoyant
211 particles.

212 A simple example of aggregation is given by Haller and Sapsis (2006), who argue that the
213 elliptical center of a steady, non-divergent 2d eddy, with $\vec{g} = |\vec{\Omega}|=0$, acts as an attractor for
214 buoyant particles. Here Q_a (now $=Q_r$), is ostensibly positive near the elliptical center of the
215 eddy, corresponding to contraction of the phase space of the rigid particle motion. Since the
216 central fixed point of the velocity field of the eddy is also a fixed point of the slow manifold
217 particle velocity (4), buoyant particles initiated about the center should migrate towards the
218 center. If the eddy is inviscid and its streamlines are circular, then the pressure and azimuthal
219 velocity are related by the cyclostrophic balance $\frac{1}{\rho_f} \frac{\partial p}{\partial r} = \frac{u_\theta^2}{r}$ so that $2Q_r = \frac{1}{\rho_f} \left(\frac{1}{r} \frac{\partial p}{\partial r} + \frac{\partial^2 p}{\partial r^2} \right)$, and



220 for an eddy in solid body rotation ($u_\theta = \Gamma_s r$), $2Q_r = \frac{1}{\rho_f} \left(\frac{1}{r} \frac{\partial p}{\partial r} + \frac{\partial^2 p}{\partial r^2} \right) = 2\Gamma_s^2$. As suggested in
221 Figure 1a, a small concentration of particles indicated by the cross hatched area shrinks as it
222 moves towards the center of the eddy. The contraction is partially due to the geometric effect of
223 movement towards smaller radius (term $\frac{1}{r} \frac{\partial p}{\partial r}$) but also due to the fact that the pressure gradient
224 decreases to zero as the center is approached and thus the inner edge of the path moves more
225 slowly inward than the outer part (term $\frac{\partial^2 p}{\partial r^2}$). In the case of solid body rotation the two terms
226 contribute equally. A second example (Fig. 1b) is of an eddy with an azimuthal velocity given
227 by $u_\theta = \Gamma_c r^{1/2}$. Here $\frac{\partial^2 p}{\partial r^2} = 0$ and $2Q_r = \frac{1}{\rho_f} \left(\frac{1}{r} \frac{\partial p}{\partial r} \right) = \Gamma_c^2 / r > 0$, so the contraction of the patch
228 is entirely due to the geometric effect of its movement towards smaller radius. The most curious
229 case is that of a point vortex: $u_\theta = \Gamma_p r^{-1}$, for which $2Q_r = \frac{1}{\rho_f} \left(\frac{1}{r} \frac{\partial p}{\partial r} + \frac{\partial^2 p}{\partial r^2} \right) = \frac{\Gamma_p^2}{r^4} - \frac{3\Gamma_p^2}{r^4} < 0$. Here
230 the vorticity is zero away from the eddy center and the velocity field is dominated by strain. The
231 pressure gradient *increases* as the center of the vortex is approached, meaning that the inner part
232 of the patch moves towards the center more rapidly than the outer portion (Fig. 1c) and this
233 tendency (quantified by the factor $-\frac{3\Gamma_p^2}{r^4}$) surpasses the tendency towards geometrical contraction
234 (quantified by the factor $\frac{\Gamma_p^2}{r^4}$). The phase space of the particle motion thus expands as particles are
235 drawn towards the center of the vortex. This behavior is made possible by the singularity at the
236 center, and although this feature is artificial, point vortices are often used in idealized models of
237 fluid flow and will act as sinks or “black holes” for buoyant particles even though $2Q_r < 0$.
238 The sign of Q_a is clearly not the whole story and does not encompass the effects of boundaries.
239 For example, consider the fate of heavy ($\rho_f < \rho_p$) particles in the eddy show in Fig. 1a. The



240 particles will migrate outward in each case, and no interior attraction will occur unless the eddy
241 is surrounded by a rigid boundary, which would then act as an attractor.

242 In the next section, we will consider a more general, 3D, eddy-like circulation: one that has both
243 vertical and horizontal components of vorticity, time dependence, and a variety of vortical
244 structures that act as candidates for attraction. Our model is based the incompressible flow in a
245 rotating cylinder (Greenspan, 1986), which has been studied in many configurations by
246 numerous authors as a models of ocean circulation, ocean eddies, and industrial processes, and
247 can be easily set up in the laboratory setting. In its original configuration the cylinder rotates
248 about a vertical axis at a constant (positive) angular velocity ($\vec{\Omega} = \Omega \vec{k}$), and the lid, which is in
249 contact with the fluid, rotates with a slightly greater angular speed. The differential rotation sets
250 up an azimuthal circulation in the horizontal and an overturning circulation in the vertical.
251 (Overturning is observed in ocean eddies as well and Ledwell et al. (2008) present an example.)
252 The steady, axially symmetric state that is established will be our first object of investigation. A
253 steady but asymmetric perturbed variant can be established by moving the axis of rotation of the
254 lid away from the axis of rotation of the cylinder, and this offset can also be varied in order to
255 induce time dependence. Fountain et al. (2000) set a similar situation up in a laboratory cylinder
256 using a submerged impeller that can be tilted, rather than the differentially rotating lid that can be
257 shifted, to establish an asymmetric disturbance flow. The authors discussed the Lagrangian
258 characteristics of the undisturbed flow and demonstrated the existence of secondary vortical
259 structures generated when the flow is perturbed. Pratt et al. (2014) reproduced similar structures
260 using a primitive equation simulation and explored the rich assembly of chaotic regions and non-
261 chaotic vortical structures as function of the Ekman and Rossby numbers of the flow. The time-
262 dependent version of the rotating cylinder flow and a theory describing the resulting vortical



263 structures were discussed by Rypina et al. (2015), who based their examples on a
264 phenomenological model that reproduced many of the qualitative features of the numerically-
265 obtained velocity field. In dimensionless Cartesian coordinates, the model velocity field is given
266 by

$$267 \quad u^{(x)} = -bx(1 - 2z) \frac{r_0 - r}{3} - ay(c + z^2) + \varepsilon \left[y(y - y_0 + \gamma \cos(\sigma t)) - \frac{r_0^2 - r^2}{2} \right] (1 - \beta z), \quad (9a)$$

$$268 \quad u^{(y)} = -by(1 - 2z) \frac{r_0 - r}{3} + ax(c + z^2) - \varepsilon x(y - y_0 + \gamma \cos(\sigma t))(1 - \beta z), \quad (9b)$$

$$269 \quad u^{(z)} = bz(1 - z) \frac{2r_0 - 3r}{3}, \quad (9c)$$

270 in which $r = (x^2 + y^2)^{1/2}$ and r_0 is the cylinder radius. The velocity field consists of a steady,
271 axially symmetric flow of strength a with an overturning circulation of strength b . To this
272 symmetric state one can add an asymmetric, possibly unsteady and depth dependent, perturbation
273 of amplitude ε (not to be confused with the Stokes number $\tilde{\varepsilon}$). The perturbation is quantified by
274 an offset parameter y_0 that introduces axial asymmetry in the velocity field, a frequency σ , and
275 an amplitude β for linear depth dependence and an amplitude γ for the time dependence. For the
276 case of axially symmetric, steady flow ($\varepsilon = 0$) the horizontal velocity field, in cylindrical
277 coordinates, becomes

$$278 \quad u^{(r)} = -br(1 - 2z) \frac{r_0 - r}{3} \quad (10a)$$

279 and

$$280 \quad u^{(\theta)} = ar(c + z^2), \quad (10b)$$



281 where θ is the azimuthal angle. Table 1 lists the parameter values used for each numerical
282 experiment.

283 In the steady, symmetric configuration, each fluid trajectory is confined to the surface of a torus
284 as it winds around the cylinder. The typical torus is associated with quasi-periodic trajectories
285 and any such trajectory, followed for a sufficient length of time, will sketch out the torus in 3D.
286 Fig. 2b contains several examples of such tori and Fig. 2a shows the corresponding Poincare
287 map, made by marking the crossing points of trajectories through a vertical slice through the
288 cylinder. After a large number of crossings each quasi-periodic trajectory traces out the cross
289 section of the torus on which it lives. The tori are nested within each another, with a single,
290 horizontal, periodic trajectory located at the center of the nest. Certain tori contain periodic
291 trajectories, and these will show up as a finite number of dots on the Poincare map. Because of
292 this geometry, the motion of fluid parcels is most naturally described in terms of action-angle-
293 angle variables, where the action, I , acts a label for a particular torus and is constant following
294 each trajectory, and the two angle variables, $\tilde{\theta}$ and ϕ , define the location of a parcel on the torus.
295 Here $\tilde{\theta}$ is an azimuthal angle that differs from the above cylindrical coordinate θ in how its
296 origin is defined, while the ‘poloidal’ angle ϕ wraps around the cross-section of each torus. The
297 coordinate are non-orthogonal but are defined in such a way that the angular velocities, $\Omega_{\tilde{\theta}}$ and
298 Ω_{ϕ} , are also constant following a trajectory. The explicit transformations to the action-angle-
299 angle variables are given in Mezic and Wiggins (1994).

300 When the symmetric RC flow is perturbed by a small, steady, symmetry-breaking perturbation,
301 as controlled by the parameters ε and y_o in (9), the tori that are populated by periodic orbits
302 potentially become resonant and break up, resulting in chaotic motion of fluid parcels in the



303 vicinity (Fig. 2d-i). Tori with quasiperiodic orbits deform but stay intact. Examples are discussed
304 by Fountain et al. (2000) and Pratt et al. (2013), and the latter found that chaos generally
305 dominates in a large region that includes the central axis of the cylinder and extends around the
306 boundaries of the cylinder. Away from this region the space is occupied by tori that have
307 survived the perturbation, and these are sandwiched between tori that have broken up and created
308 braided regions of chaos. The breakup of a torus also gives rise to new tori that appear as islands
309 in the Poincare maps (Fig. 3d and 3g) and these contain non-chaotic trajectories. The number of
310 islands can be predicted by a theory that decomposes the symmetry-breaking perturbation into
311 Fourier modes, written in the $(I, \tilde{\theta}, \phi)$ coordinates, with wave numbers n and m in the $\tilde{\theta}$ and ϕ
312 direction. If the angular velocities $\Omega_{\tilde{\theta}}$ and Ω_{ϕ} characterizing the trajectories on a particular torus
313 satisfy the resonance condition $n\Omega_{\tilde{\theta}} + m\Omega_{\phi} = 0$ for some n and m , equivalent to the trajectories
314 on that torus being periodic, then that torus will break up and a new set of invariant tori (islands)
315 will form. Running through the center of the islands will be a periodic trajectory that will execute
316 n azimuthal cycles to every m poloidal (overturning) cycles. In the case shown in Fig. 3a,
317 $n=m=1$, so the periodic trajectory circles the cylinder horizontally once for each overturning
318 cycle: a so-called 1:1 resonance.

319 If the symmetry breaking perturbation is quasi-periodic in time, with underlying frequencies σ_i ,
320 the resonance condition for the breakup of a torus becomes $n\Omega_{\tilde{\theta}} + m\Omega_{\phi} + l_i\sigma_i = 0$, where l_i 's
321 are integers (Rypina, et al. 2015). Unlike the resonance condition for the steady perturbation,
322 which is only satisfied on tori foliated by periodic trajectories, this new resonant condition may
323 be satisfied on tori that have quasi-periodic orbits, and the resonant islands that form will have a
324 shape and location that vary in time. An example (Fig. 2g,h) of the case of a resonance with a
325 single-frequency (i.e., time-periodic) perturbation shows a number of resonant islands. These



326 features vary in time, recovering their shape and location periodically, and the snapshots shown
327 are obtained by strobing the trajectories in 3D and at the forcing frequency. The green and blue
328 islands in Fig. 2h have resulted from the breakup of tori with quasiperiodic trajectories, and
329 center of the island corresponds to a closed material curve that is populated with quasiperiodic
330 trajectories.

331 **III. Results**

332 Aggregation of rigid particles will occur in presence of an attractor, an object with a dimension
333 < 3 to which particles tend asymptotically in time. We are most interested in attractors that occur
334 in the interior of the rotating cylinder, and are set up by the background circulation, as opposed
335 to the physical boundaries of cylinder. We will see that a closed material contour consisting of
336 periodic orbits near the core of the nested tori in the steady symmetric case act as an attractor for
337 slightly buoyant particles, and that similar material contours consisting of periodic or
338 quasiperiodic orbits near the centers of the resonant islands in the asymmetric cases can play the
339 same role. We will explore three cases in increasing complexity, beginning with steady flows
340 with axial symmetry, and proceeding to steady, asymmetric flows and finally unsteady
341 asymmetric flows.

342 The search for attractors is motivated by the hypothesis that for cases of strong drag, where the
343 particle velocity lies close to the fluid velocity, a periodic orbit for the particle motion will exist
344 in the vicinity of a periodic trajectory for the fluid motion, and that if $Q_a > 0$ in a region
345 surrounding the latter, that it should attract particles. For the time-dependent case, we extend the
346 search to included closed material contours that contain recirculating particles and that vary
347 periodically in time.



348 (a) steady, axially-symmetric 3D flows

349 The fluid velocity field for this case is given by Eqs. 9c and 10, and these indicate that the
 350 location of the horizontal, periodic trajectory living at the center of the nested tori, is given by
 351 $r = 2r_o/3$ and $z = \frac{1}{2}$. It is natural to ask whether a periodic trajectory for rigid particles also
 352 exists nearby. In the slow-manifold approximation, the steady radial, azimuthal and vertical
 353 particle velocities are obtained by writing (4) in cylindrical coordinates, leading to

$$354 \quad v^{(r)} = u^{(r)} + \tilde{\varepsilon} \left(\frac{3R}{2} - 1 \right) \left[\left(u^{(r)} \frac{\partial}{\partial r} + u^{(z)} \frac{\partial}{\partial z} \right) u^{(r)} - u^{(\theta)} \left(2\Omega + \frac{u^{(\theta)}}{r} \right) - \Omega^2 r \right] \quad (11a)$$

$$355 \quad v^{(\theta)} = u^{(\theta)} + \tilde{\varepsilon} \left(\frac{3R}{2} - 1 \right) \left[\left(u^{(r)} \frac{\partial}{\partial r} + u^{(z)} \frac{\partial}{\partial z} \right) u^{(\theta)} + u^{(r)} \left(2\Omega + \frac{u^{(\theta)}}{r} \right) \right] \quad (11b)$$

$$356 \quad v^{(z)} = u^{(z)} + \tilde{\varepsilon} \left(\frac{3R}{2} - 1 \right) \left[\left(u^{(r)} \frac{\partial}{\partial r} + u^{(z)} \frac{\partial}{\partial z} \right) u^{(z)} + g \right] \quad (11c)$$

357 Position of attracting periodic orbit; approximate analytical expression on a slow manifold

358 Searching for points $r = r_c$ and $z = z_c$ for which $v^{(r)} = v^{(z)} = 0$, and that lie in the proximity of
 359 the horizontal trajectory of the flow, we introduce

$$360 \quad r_c = \frac{2r_o}{3} + \tilde{\varepsilon} \left(\frac{3R}{2} - 1 \right) \tilde{r} \quad \text{and} \quad z_c = \frac{1}{2} + \tilde{\varepsilon} \left(\frac{3R}{2} - 1 \right) \tilde{z}.$$

361 Substituting into the right-hand sides of (11a,c) and setting both to zero results, after neglect of
 362 $O(\tilde{\varepsilon}^2)$ terms, in

$$363 \quad r_c = \frac{2r_o}{3} + \tilde{\varepsilon} \left(\frac{3R}{2} - 1 \right) \frac{g}{b} r_o \quad (12a)$$

364 and

$$365 \quad z_c = \frac{1}{2} + \frac{9}{2br_o} \tilde{\varepsilon} \left(\frac{3R}{2} - 1 \right) \left[\Omega^2 + a \left(c + \frac{1}{4} \right) \left(2\Omega + a \left(c + \frac{1}{4} \right) \right) \right]. \quad (12b)$$



366 For the parameters $a>0$ and $b>0$, circulation is cyclonic with upwelling in the center of the
367 cylinder, and $(3R/2)-1>0$ for buoyant particles, so the $O(\tilde{\epsilon})$ corrections are positive and the
368 periodic particle orbit lies at larger radius and elevation than the periodic fluid orbit. Note also
369 from Eq. (11b) that the azimuthal velocity component of the rigid particle on the periodic orbit is
370 equal to that of the fluid.

371 An explanatory sketch (Fig. 3) shows the position of the periodic orbit of the rigid particle
372 relative to that of the periodic orbit of the fluid. Since the rigid particle is buoyant, it can
373 maintain its level z only if it is situated in a region where the vertical fluid velocity is <0 , here to
374 the right of the fluid periodic orbit. Also, the horizontal pressure gradients associated with the
375 centripetal acceleration associated with the frame rotation (term $\Omega^2 r$), the Coriolis acceleration
376 (term $2\Omega u^{(\theta)}$), and the centripetal acceleration due to the azimuthal velocity $u^{(\theta)^2}/2r$ are all
377 positive for this flow, so that low pressure exists at $r=0$ and the rigid particle is forced
378 horizontally inward. To remain stationary the particle must sit in a region where the radial
379 velocity of the fluid is outward. In this manner, the periodic trajectory exists at a location where
380 the forces of inertia, buoyancy and added mass can be countered by the drag due to the
381 background flow. If we fix all other parameters and increase Ω through positive values, the term
382 multiplying $\tilde{\epsilon}$ in (12b) will become dominated by the Ω^2 term and will grow without bound and
383 the periodic trajectory may cease to exist. At the same time, a periodic orbit for the rigid particle
384 can always be found close to that of the fluid, regardless of the magnitudes of the parameters Ω ,
385 a , b etc., provided that the relative particle size d/L (and thus $\tilde{\epsilon}$), and/or the relative density
386 difference $\frac{(\rho_f - \rho_p)}{\rho_f}$ (and thus $\frac{3R}{2} - 1$) are made sufficiently small.

387 Position of attracting periodic orbit; conditions for the loss of periodic orbit



388 We have suggested that periodic orbits for rigid particles are encouraged when the $\tilde{\varepsilon} \left(\frac{3R}{2} - 1 \right)$
389 $\ll 1$, and in the case of Run 1 the value is .0066. A cross-sectional plot of the radial and vertical
390 components of the slow manifold particle velocity in a vertical section through the cylinder (Fig.
391 4a) shows that the periodic orbit lies at $r=.369$ and $z=.504$ (as compared to the values $r_c = .338$
392 and $z_c = .502$ predicted by (12). (The convergence of the surrounding velocity field is too weak
393 to be seen in the graphic.) If $\tilde{\varepsilon} \left(\frac{3R}{2} - 1 \right)$ is raised to the moderately small value .02, the position
394 of periodic trajectory migrates towards larger radius (Fig. 4b), the reason being that the greater
395 buoyancy (larger value of $\frac{3R}{2} - 1$) or smaller drag (larger $\tilde{\varepsilon}$) requires a larger downward fluid
396 velocity for equilibrium. Since the maximum downward fluid velocity occurs at the outer
397 cylinder wall (see Eq. 9c) the position of the periodic orbit continues to migrate outward and is
398 lost (Fig. 4c) when $\tilde{\varepsilon} \left(\frac{3R}{2} - 1 \right)$ exceeds a value close to 0.3.

399 *Position of periodic orbit in numerical simulations:*

400 The slow-manifold reduction yields to prediction (Eq. 12) of the position of the attracting
401 material contour for slightly buoyant particles. We can compare this prediction to what is
402 observed in numerical simulations using the Maxey-Riley equations (1) and (2) over a range of
403 particle size d (and thus $\tilde{\varepsilon}$) and frame rotation Ω . As shown in Fig. 5, qualitative agreement with
404 the slow-manifold prediction, and the sketch in Fig. 3, holds for a very small d (when $\tilde{\varepsilon}$ is small).
405 Here the attractor in Fig. 5 is located close to the central periodic fluid parcel trajectory that lives
406 at mid-depth, $z = 0.5$ and $r = \frac{2R}{3} \approx 0.33$. As d (and $\tilde{\varepsilon}$) increases, the attractor moves
407 increasingly up and outward, and although the theory captures the trends, quantitative agreement
408 with the numerical results worsens. Also, when frame rotation Ω is increased (panel c), the



409 attractor responds by shifting up from mid-depth, again in qualitative but not quantitative

410 agreement with the slow-manifold prediction in eq. (12b).

411 *Geometry of particle trajectories and evidence of attraction in numerical simulations:*

412 If in the neighborhood of the period trajectory the Q_a function >0 , the phase space for buoyant
413 particles will contract and the periodic trajectory becomes a candidate for an attractor of such
414 particles. An example of the attraction towards the periodic orbit is shown in Figure 2c, where a
415 set of slightly buoyant particles ($\frac{\rho_p}{\rho_f} = 0.97$) has been initialized over the volume of the cylinder,
416 and eqs. (1) and (2) have been integrated forward in time to determine their subsequent
417 trajectories. Each trajectory is shown using a unique color. It can be seen that the particles
418 aggregate within a ring-like structure of decreasing thickness in the general vicinity of the
419 periodic orbit of the fluid flow.

420 *Basin of attraction – relationship to Q_a :*

421 To map out the basin of attraction for the particle periodic orbit we first consider the region over
422 which phase space contraction for the buoyant particles (i.e. $Q_a > 0$) occurs. This region is shown
423 in Fig. 6a for the current example, along with the streamlines of the fluid overturning stream
424 function. Much of the fluid flow recirculates entirely within the region of positive Q_a , whereas
425 some of the outer streamlines cross the boundary (thick contour) between positive and negative
426 Q_a . If it were the case that rigid particles exactly followed streamlines of the fluid overturning
427 circulation, then net contraction or expansion of phase space along a rigid particle trajectory
428 would depend on the sign of the time-integrated value of Q_a along streamlines. The $Q_a=0$
429 contour, shown by a bold contour in each frame of Fig. 6, might then approximately delineate the



430 basin of attraction for rigid particles. In the slow-manifold approximation, where rigid particle
431 velocities lie close to the fluid velocities, the $Q_a=0$ contour might continue to do so.

432 To test this conjecture, we locate the basin of attraction in the numerical simulations by releasing
433 buoyant particles at various locations in the cross-section $0 < x < r_o$ and $0 < z < 1$, integrating the
434 subsequent trajectories over many overturning cycles, and recording the position (x_{final} and
435 z_{final}) of each particle where it crosses the same plane the final time (i.e., recording final
436 crossing with the Poincare section). The values of z_{final} as a function of initial particle position
437 are mapped in Fig. 7a, where the large green area corresponding to $z_{final} \cong 0.5$ indicates the
438 region from which particles are attracted. Only particles initiated near the central axis of the
439 cylinder, and close to the cylinder boundaries lie outside this region, and these rise to the surface
440 of the cylinder, contact the upper lid, and are no longer followed. It can be seen that the green
441 area in Fig. 7a has an oval shape that somewhat resembles the overturning streamlines at small x
442 in the central part of the cylinder, but extends to near the top, bottom and outer cylinder
443 boundaries at larger x . Thus the $Q_a=0$ contour provides a rough indication of the size and shape
444 of the basin of attraction, but misses some important details.

445 Basin of attraction – dependence on Ω

446 We have seen that the location of the periodic orbit that acts as an attractor for buoyant particles
447 shifts up and out in response to increasing frame rotation Ω (Fig. 5c). In Fig. 8 we indicate the
448 corresponding changes in the extent of the basin of attraction with respect to changing Ω by re-
449 computing Fig. 8a with $\Omega = 0.3, 1, \text{ and } 10$. The two smaller Ω values (0.3 and 1) correspond
450 roughly to Rossby numbers $a/2\Omega$ of about 1 and 0.2, i.e., are representative of the ocean
451 submesoscale and mesoscale flows. The Q_a -functions for these cases are plotted in Fig. 6b-c.



452 Most submesoscale eddies are going to tend to have $u^{(\theta)}/r$ about the same magnitude as Ω
453 (except on the equator) and mesoscale eddies will have $u^{(\theta)}/r \ll \Omega$. The results in Fig. 8
454 suggest that, while the basin of attraction does shrink slightly with increasing Ω , this dependence
455 is weak. The main difference between the three numerical runs in Fig. 8 is in the associated
456 attraction time, which gets significantly shorter for larger values of Ω . This is explored in more
457 detail below.

458 Attraction time:

459 It follows from Eq. (6) that the attraction time towards the periodic orbit should scale as $T_a =$
460 $\left[2\tilde{\epsilon} \left(\frac{3R}{2} - 1\right) Q_a\right]^{-1}$ where $Q_a = \frac{1}{2} \left(|\vec{\zeta}_a|^2 - |S|^2\right)$ with $\vec{\zeta}_a = \vec{\zeta}_r + \overline{2\Omega}$. Thus, for $\vec{\zeta}_r \geq 0$, as in
461 most of our numerical runs (except Experiment 1e), attraction time decreases with increasing Ω
462 for positive $\Omega \geq 0$. For negative $\vec{\zeta}_r$, which corresponds to the reversed direction of the flow in
463 our simulations (Experiment 1e), an increase in Ω will initially slow the attraction by decreasing
464 the magnitude of $\vec{\zeta}_a$ all the way to 0, at which point the periodic orbit will lose its attraction
465 properties, but then will speed up the attraction as Ω is further increased. This trend is confirmed
466 numerically in Fig. 9, where for the flow parameters corresponding to the “reversed flow” run in
467 Table 1 (Experiment 1e, with $\vec{\zeta}_r < 0$), we release a sample trajectory within the basin of
468 attraction and plot its z-coordinate as it winds around the can and eventually approaches the
469 attracting periodic orbit. As anticipated, the attraction time initially increases as Ω is increased
470 from 0 to 0.6, but then decreases as Ω is further increased to 2.

471 Disappearance of the subsurface attractor when $\tilde{\epsilon}$ becomes too large:

472 Finally, to illustrate the disappearance of the subsurface attractor when $\tilde{\epsilon}$ becomes too large, in
473 Fig. 10, we contrast 2 numerical simulations with the same flow parameters (corresponding to



474 the “slow overturn” run 1c in Table 1) but different particle diameters, $d = 10^{-3}$ vs $d = 5 \times$
475 10^{-4} . For larger d , the subsurface periodic orbit for rigid particles is no longer present within the
476 can, leading to all particles rising up to the surface (Fig. 10b). For smaller d , the periodic orbit is
477 still present and acts as an attractor for rigid particles over a significant portion of the can (green
478 region in Fig. 10a). We note that this run is more typical of oceanic mesoscale or submesoscale
479 eddies, where the overturning component of circulation is weak in comparison to the horizontal
480 swirl.

481 (b) steady non-symmetrically perturbed case

482 We now consider a case in which the axial symmetry of the steady flow has been broken, here
483 through a change in the perturbation amplitude parameter ε from zero to 0.25, and in the offset
484 parameter y_o from 0 to -0.2 in the Eqs. 9a,b. The fluid velocity field now contains something like
485 a stationary, “mode-1” azimuthal wave in the horizontal velocity field.

486 The resulting Lagrangian structure (Fig. 2d and e) has a sea of chaos that covers the near-axial
487 and outer regions of the cylinder, where no unbroken tori anymore exist. Within this chaotic sea
488 is a region containing a nest of unbroken tori that surround a central periodic orbit. This orbit has
489 evolved from the central periodic orbit of the symmetry case and is now tilted. Within the nest of
490 unbroken tori there exist resonant layers, in which new tori have arisen, and the most prominent
491 is the “island” that is centered near $x=0.4$ and $z=0.2$ in the right-half (and near $x=0.4$ and $z=0.2$ in
492 the right half) of Fig. (2d). We further note that this center lies within the region of positive Q_a
493 (Figure 6b). The island corresponds to the yellow tori in Fig. 3e and is produced by a 1:1
494 resonance, so that the periodic trajectory running through its center executes one complete
495 azimuthal cycle and one overturning cycle before connecting back onto itself. Thus, in this
496 steady asymmetric configuration, we now have 2 periodic orbits of the fluid flow – the central



497 slightly-tilted periodic orbit near mid-depth (that evolved from the central horizontal periodic
498 orbit of the axisymmetric flow) and a new periodic orbit running through the center of the
499 resonant island (resulting from the break-up of the resonant torus satisfying $\Omega_{\bar{\theta}} + \Omega_{\phi} = 0$).

500 We speculate that for sufficiently small ε a periodic orbit for the rigid particle motion exists in
501 the vicinity of each of the 2 periodic orbits of the fluid flow. This conjecture is difficult to prove
502 due to a complex geometry, leading to centrifugal forces that act in different directions at
503 different locations along the particle path. For now we simply search for the supposed attractors
504 by releasing particles and following their trajectories.

505 As shown in Fig. 2f, separate attractors arise in the vicinity of two periodic orbits. The first
506 appears as a ring-like structure (purple core) lying near the center of the original nested tori and
507 the second is a similar feature with a red core near the center of the resonant island. The two are
508 chained together and each has its own basin of attraction (Fig. 7c): the first consisting of a
509 roughly elliptical patch (inner green region) in the x-z-plane, which corresponds of a slice
510 through a tube-like structure in 3D, and the second consisting on an annular (blue) region that
511 surrounds the green region and that occupies a relatively larger volume.

512 In order to check that attraction of slightly buoyant, rigid particles towards periodic orbits
513 located near the centers of the resonant islands in the perturbed flow is not limited to the case of
514 the 1:1 resonance, in an additional simulation (Fig. 11, experiment 2c in Table 1), we adjusted
515 the background flow parameter b in Eqs. (9), which is responsible for the overturning strength, to
516 create a 2:1 resonance instead of a 1:1 resonance, as in the original run. In this case, the resonant
517 torus breaks down giving rise to a 2-island chain on the corresponding Poincare section (Fig.
518 11a), and the periodic orbit that goes through the centers of both islands completes 2 full cycles



519 in azimuth and 1 complete cycle in vertical before connecting onto itself. Also, as in the original
520 run, a second slightly-tilted periodic orbit still exists near mid-depth of the can. When buoyant
521 particles are released into this flow, two attractors arise, corresponding to the 2 periodic orbits –
522 one near mid-depth (purple core in Fig. 11c) and another in red near the center of the 2:1
523 resonant island.

524 *Shift in position of the periodic orbit associated with a resonant island as a function of flow and*
525 *particle parameters, and frame rotation*

526 The position of the attracting periodic orbit for rigid particles that is located within the resonant
527 islands (we will refer to it as the resonant periodic orbit) in the asymmetrically-perturbed flow
528 depends both on the perturbation strength (via ε), on the flow and particle parameters (via $\tilde{\varepsilon}$), and
529 on the frame rotation Ω . Specifically, this resonant periodic orbit for the rigid particles will shift
530 away from the corresponding periodic trajectory of the fluid flow as $\tilde{\varepsilon}$ and Ω are increased. The
531 same is true for the slightly-tilted central attracting periodic orbit near mid-depth. This is
532 qualitatively similar to the shifting of the central periodic orbit up and out from $z = 0.5$,
533 $r = 0.34$ in the axisymmetric flow in response to changing $\tilde{\varepsilon}$ and Ω , which we explored in detail
534 the previous section both analytically (Eqs. 12) and numerically (Fig. 3-5).

535 In order to numerically illustrate the shift in the position of the attracting periodic orbits, we
536 present (Figs 12 and 13) numerical simulations in the steady perturbed flow configuration for 3
537 values of d (and thus $\tilde{\varepsilon}$) and 3 values of Ω . As both parameters increase, the attractors move
538 away from the corresponding periodic orbits of the fluid flow. This shift is evident from the
539 change in the color of the attraction basins in (a,d,g) and from the location of the yellow cloud of
540 dots in (c,f,i) in Figs. 12-13. Increases in $\tilde{\varepsilon}$ and Ω also lead to the shrinkage of the attraction



541 basins for both attractors and to a faster convergence rate, as is evident from the tighter cloud of
542 yellow dots in (c,f,i), as discussed in more detail below. The basin of attraction for the central
543 attractor – the green region in Fig. 12 – seems to shrink faster than the basin of attraction for the
544 resonant attractor (the blue-ish region) as d increases, so when d is increased from 2×10^{-3} to
545 3×10^{-3} , the central attractor vanishes, whereas the resonant attractor is still present (Fig. 12g).
546 On the other hand, the increase in Ω (Fig. 13) causes a faster shrinkage of the basin of attraction
547 for the resonant attractor than for the central attractor, so when Ω is increased from 2 to 5 in Fig.
548 13g, the resonant attractor disappears, whereas the central attractor is still present. Figs. 12g,h,i
549 (and Fig. 13g,h,i) show cases where this threshold has been exceeded, and one of the attractors
550 has been lost, whereas the other is still present.

551 Attraction time:

552 Similar to the unperturbed flow, the attraction time for attractors in the steady, perturbed flow
553 may still scale as $T_a = \left[2\tilde{\varepsilon} \left(\frac{3R}{2} - 1 \right) Q_a \right]^{-1}$, provided that Q_a is regarded as a typical value
554 within the corresponding basin of attraction. The predicted decrease in attraction time with
555 increasing $\tilde{\varepsilon}$ and Q_a is evident from the numerical simulations in Figs. 12-13, where in (c,f,i) we
556 color-coded trajectory crossings with the x-z Poincare plain by time, with blue/yellow
557 corresponding to initial/final time. For smaller values of $\tilde{\varepsilon}$ and Ω , we observe a wider and more
558 diffuse cloud of dots (because trajectories wind around the can many times before approaching
559 the attractor), whereas as $\tilde{\varepsilon}$ and Ω increase, the clouds at comparable times become denser and
560 more compact around the attractors.

561 Basin of attraction



562 For the slightly-tilted central periodic orbit located within the central non-chaotic region near
563 mid-depth in Fig. 2f, we observe that the basin of attraction – green region in Fig. 7b – extends
564 roughly from the location of the periodic orbit to the edge of the central non-chaotic region (that
565 is foliated by discretely sampled closed curves in Fig. 2d). Note that as $\tilde{\epsilon}$ increases, the attracting
566 periodic orbit moves away from the center of this non-chaotic region towards its edge, leading to
567 the shrinkage and eventual disappearance of the corresponding basin of attraction, shown by the
568 green regions in Fig. 12a,d,g).

569 Similarly, in all of our numerical simulations, we observe that for the resonant attracting periodic
570 orbit running through the resonant islands, the basin of attraction seems to cover the region
571 between the orbit and the edge of the corresponding resonant island. An analytical expression for
572 the width of the (non-degenerate) resonant island in the fluid flow (Pratt et al., 2014) predicts

573 that $\Delta I = \sqrt{\frac{\epsilon F_{nm}^0(I_0)}{\left(n \frac{d^j \Omega_\phi}{dI^j} + m \frac{d^j \Omega_\theta}{dI^j}\right)_{I_0}}}$, where ΔI is the deviation in the action coordinate away from I_0 , the

574 value of action at the resonant torus (i.e., at the center of the island). This width depends on the
575 strength of the perturbation ϵ , the order of the resonance (via n and m in the resonance

576 condition), the background flow (via $\frac{d^j \Omega_\phi / \theta_1}{dI^j}$), and the structure of the perturbation (via $F_{nm}^0(I_0)$).

577 This expression could be used as an upper limit on the extent of the basin of attraction. However,
578 because the attracting periodic orbit will move away from the center of the island towards its
579 edge as $\tilde{\epsilon}$ and Ω increase, the basin of attraction for the resonant attractor (blue region in Figs.
580 12a,d and 13a,d) becomes increasingly smaller than ΔI . One might speculate, then, that the
581 attractor will completely disappear when the attracting periodic orbit reaches the edge of the
582 resonant island. This is the case in Figs. 13g where the resonant attractor is no longer present.



583 (c) non-steady, non-symmetrically perturbed case

584 The final case that we will consider is one in which the perturbation is asymmetric and varies
585 periodically in time. The chosen perturbation frequency, $\sigma = 2\pi/9.1$, causes 2 strong additional
586 resonances (compared to the steady perturbed case) – one with $n=0$, $m=1$, and $l=1$ (i.e., with a
587 torus whose overturning frequency is equal to the perturbation frequency) that is shown in blue
588 in Fig. 2g,h and is located near the outer edge of the central non-chaotic region, and another
589 resonance, shown in green in Fig. 2g,h, with $n=1$, $m=1$, and $l=1$, which is located between the
590 central non-chaotic region and the larger $n=1$, $m=1$ resonant island (that was present in the steady
591 case as well). Both of these new resonant structures are time dependent, their shape and position
592 recurring periodically. For example, the blue island, which looks like a crescent moon pointing
593 upward on the Poincare section at $t=0$, becomes a crescent moon pointing downward at time
594 4.55. The movement of the green island is a more complex, as it turns both in azimuth and
595 vertical, making one complete loop over 9.1 time units. Because of the time-dependence,
596 trajectories must be strobed at the forcing frequency σ in order to capture ‘snapshots’ of their
597 forms as they recur at a particular phase in the time cycle. At the center of each feature is a
598 closed material curve that also varies periodically. Where the island has emerged from the
599 breakup of a torus with quasiperiodic orbits, the individual trajectories that populate the material
600 curves are themselves quasiperiodic.

601 Particle trajectory computations in this case confirm that the purple, red and green islands give
602 rise to attractors (Fig. 3i), whereas the blue island does not. In fact, particles that are released in
603 the blue region converge towards the attractor that lies near the purple region. This is also
604 indicated by the basin of attraction of the central attractor extending across the space occupied by
605 the blue resonant island in Fig. 7c.



606 **IV. Discussion**

607 We have considered attraction phenomena for small, spherical, buoyant, rigid particles in a three-
608 dimensional rotating cylinder flow with azimuthal rotation and overturning. The aim has been to
609 gain insights into the behavior of slightly buoyant microplastic particles in 3D vortex flows that
610 qualitatively resemble ocean eddies. The particle motion is governed by a simplified version of
611 the Maxey-Riley equations (accounting for inertia, buoyancy and simplified quantification of
612 drag and added mass), and, approximately, by the slow-manifold reduction of these equations.

613 We have explored a steady axisymmetric rotating cylinder flow and a steady flow with its axial
614 symmetry broken. In all cases, we have observed emergence of subsurface attracting structures
615 that lead to the aggregation of buoyant particles towards them. We have linked these attractors to
616 the periodic orbits of rigid particles that exist in a region of net contraction of the phase space of
617 the particle motion. The slow manifold equations suggest that periodic orbits for rigid particles
618 exist near periodic orbits of the underlying fluid flow, provided the drag is sufficiently strong
619 (Stokes number $\ll 1$).

620 We have also explored one case of an axially asymmetric and time-periodic flow, with focus on
621 the resonant “islands” that arise due to the time-dependence. At the center of such islands are
622 closed material contours composed of quasi-periodic orbits of the fluid flow. One such structure
623 has nearby attractor, also a closed material contour of quasiperiodic orbits for rigid particles,
624 while a second example does not. A detailed explanation awaits formulation of a quantitative
625 theory, something that is beyond the scope of the present paper and that will be presented in a
626 future work.



627 We have observed that the disappearance of an attractor, which can occur as the result of
628 increasing particle size or frame rotation, coincides roughly with the displacement of the position
629 of the attractor to the outer edge of the resonant island from which it sprang. Whether this purely
630 geometric observation forms the basis for a general criterion for the loss of attraction is
631 unknown, as a dynamical justification is needed.

632 **Acknowledgements:** Work supported by the NSF grant OCE# 2124210 and ONR CALYPSO
633 grants #N000141812417 and #N000141812165.

634 **Data Availability Statement:** No observational data was used. Details of the numerical
635 simulations using an analytical vortex model are provided in text.

636 **Author Contribution Statement:** IR led the overall effort and performed most of the numerical
637 simulations, LP contributed towards the theoretical understanding and interpretation of the
638 results, MD participated in the overall effort.

639 **Competing interests Statement:** no competing interests

640

641

642

643

644

645



646

647

648 **References**

649 Basset, A. B. (1988). *Treatise on Hydrodynamics*, Deighton Bell, London, Vol. 2, Chap. 22, pp.

650 285-297.

651 Beron-Vera, F. J., M. J. Olascoaga and R. Lumpkin, 2016. Inertia-induced accumulation of

652 flotsam in the subtropical gyres. *Geophys. Res. Lett.*, 43, 12228-12233,

653 <https://doi.org/10.1002/2016g1071443>.

654 Beron-Vera, F. J., M. J. Olascoaga and P. Miron, 2019. Building a Maxey-Riley framework for

655 surface ocean inertial particle dynamics. *Phys. Fluids* 31; doi: 10.1063/1.5110731.

656 Beron-Vera, F.J., 2021. Nonlinear dynamics of inertial particles in the ocean: From drifters and

657 floats to marine debris and Sargassum. *Nonlinear dynamics*, 103(1), pp.1-26.

658 Boussinesq, J. (1903) *Theorie Analytique de la Chaleur*, L'Ecole Polytechnique, Paris, Vol.2, p.

659 224.

660 Brandt, L. and F. Coletti (2022) Particle-Laden Turbulence: Progress and Perspectives. *Ann.*

661 *Rev. Fluid Mech.* 54, 159-189. <https://doi.org/10.1146/annurev-fluid-030121-021103>

662 Delandmeter, P. and E. van Sebille (2019). The Parcels v2.0 Lagrangian framework: new field

663 interpolation schemes. *Geosci. Model Dev. Discuss.*, <https://doi.org/10.5194/gmd-2018-339>

664 DiBenedetto, M. H., N. T. Ouellette, and J. R. Koseff, 2018a. Transport of anisotropic particles

665 under waves. *J. Fluid. Mech.* 837, 320-340, doi:10.1017/jfm.2017.853.



- 666 DiBenedetto, M.H. and Ouellette, N.T., 2018. Preferential orientation of spheroidal particles in
667 wavy flow. *Journal of Fluid Mechanics*, 856, pp.850-869.
- 668 Faxén, H., 1922. Der Widerstand gegen die Bewegung einer starren Kugel in einer zähen
669 Flüssigkeit, die zwischen zwei parallelen ebenen Wänden eingeschlossen ist. *Annalen der*
670 *Physik*, 373(10), pp.89-119.
- 671 Froyland, G., Stuart, R. M., & van Sebille, E. (2014). How well-connected is the surface of the
672 global ocean?. *Chaos*, 24(3), 033126. <https://doi.org/10.1063/1.4892530>
- 673 Fenichel, N.: Geometric singular perturbation theory for ordinary differential equations. *J. Differ.*
674 *Equ.* 31, 51–98 (1979)
- 675 Gagnol, R., 1983. The Faxén formulae for a rigid particle in an unsteady non-uniform Stokes
676 flow.
- 677 G. Haller and T. Sapsis, 2008. Where do inertial particles go in fluid flows? *Physica D*, 237, 573-
678 583.
- 679 Kelly, R., D. B. Goldstein, S. Suryanarayanan, M. B. Torielli and R. A. Handler, The nature of
680 bubble entrapment in a Lamb-Oseen vortex. *Phys. Fluids* 33, 061702;
681 <https://doi.org/10.1063/5.0053658>.
- 682 Kukulka, T., Proskurowski, G., Morét-Ferguson, S., Meyer, D. W., & Law, K. L.(2012). The
683 effect of wind mixing on the vertical distribution of buoyant plastic debris. *Geophysical*
684 *Research Letters*, 39, L07601. <https://doi.org/10.1029/2012GL051116>
- 685 Landrigan PJ, Raps H, Cropper M, Bald C, Brunner M, Canonizado EM, Charles D, Chiles TC,
686 Donohue MJ, Enck J, Fenichel P, Fleming LE, Ferrier-Pages C, Fordham, R, Gozt A, Griffin



- 687 C, Hahn ME, Haryanto B, Hixson R, Ianelli H, James BD, Kumar P, Laborde A, Law KL,
688 Martin K, Mu J, Mulders Y, Mustapha A, Niu J, Pahl S, Park Y, Pedrotti M-L, Pitt JA,
689 Ruchirawat M, Seewoo BJ, Spring M, Stegeman JJ, Suk W, Symeonides C, Takada H,
690 Thompson RC, Vicini A, Wang Z, Whitman E, Wirth D, Wolff M, Yousuf AK, Dunlop S.
691 The Minderoo-Monaco Commission on Plastics and Human Health. *Annals of Global*
692 *Health*. 2023; 89(1): 23, 1–215. DOI: <https://doi.org/10.5334/aogh.4056>
- 693 Lange, M. and E. van Sebille (2017) Parcels v0.9: prototyping a Lagrangian ocean analysis
694 framework for the petascale age. *Geosci. Model Dev.*, 10, 4175-4186.
695 <https://doi.org/10.5194/gmd-10-4175-2017>
- 696 Ledwell, J. R., McGillicuddy, D. J., and Anderson, L. A., “Nutrient flux into an intense deep
697 chlorophyll layer in a mode-water eddy,” *Deep Sea Res., Part II* 55, 1139–1160 (2008).
- 698 Maxey, M.R. and J. J. Riley, 1983. Equation of motion for a small rigid sphere in a nonuniform
699 flow. *Phys. Fluids* 26, 883.
- 700 Mountford, A. S. and M. A. Morales Maqueda (2019) Eulerian Modeling of the
701 Three-Dimensional Distribution of Seven Popular Microplastic Types in the Global Ocean.
702 *J. Geophys. Res.: Ocean*, 124, 8558-8573. <https://doi:10.1029/2019JC015050>.
- 703 Onink, V., Wichmann, D., Delandmeter, P., and van Sebille, E., 2019: The role of Ekman
704 currents, geostrophy and Stokes drift in the accumulation of floating microplastic, *Journal of*
705 *Geophysical Research: Oceans*, 124, 1474-1490, <https://doi.org/10.1029/2018JC014547>,
- 706 Okubo, A., 1970, June. Horizontal dispersion of floatable particles in the vicinity of velocity
707 singularities such as convergences. In *Deep sea research and oceanographic abstracts* (Vol.



- 708 17, No. 3, pp. 445-454). Elsevier.
- 709 Pratt, L. J., I. I. Rypina, T. Özgökmen, H. Childs, and T. Bebieva, 2014. Chaotic Advection in a
710 Steady, 3D, Ekman-Driven Circulation. *J. Fluid Mech.*, 738, 143-183,
711 DOI:10.1017/jfm.2013.583.
- 712 Rypina, I. I., L. J. Pratt, P. Wang, T. M. Ozgokmen, and I. Mezic, 2015. Resonance phenomena
713 in a time-dependent, three-dimensional, Ekman-driven eddy. *J. Chaos.*, 25, 087401,
714 <http://dx.doi.org/10.1063/1.4916086>.
- 715 Shamskhany, A., Z. Li, P. Patel and S. Karimpour. Evidence of Microplastic Size Impact on
716 Mobility and Transport in the Marine Environmnet: A Review and Synthesis of Recent
717 Research. *Front. Mar. Sci.* 8:760649. Doi: 10.3389/fmars.2021.760649.
- 718 Stokes, G. G. (1851) *Trans. Camb. Phil. Soc.* 9, 8. (*Mathematical and Physical Papers* 3,1.)
- 719 Tchen, C. M. (1947). Ph. D. thesis, Delft, Martinus Nijhoff, The Hague/
- 720 van Sebille E., C. Wilcox, L. Lebreton, N. Maximenko, B.D. Hardesty, J.A. van Franeker, M.
721 Eriksen, D. Siegel, F. Galgani, K.L. Law (2015) A global inventory of small floating plastic
722 debris *Environ. Res. Lett.*, 10 (2015), p. 124006, 10.1088/1748- 9326/10/12/124006
- 723 Wichmann, D., P. Delandmeter and E. van Sebille, 2019. Influence of Near-Surface Currents on
724 the Global Dispersal of Marine Microplastics. *J. Geophys. Res. (Oceans)*, 124(8),
725 <https://doi.org/10.1029/2019JC015328>
- 726 Weiss, J., 1991. The dynamics of enstrophy transfer in two-dimensional hydrodynamics. *Physica*
727 *D: Nonlinear Phenomena*, 48(2-3), pp.273-294.



| Experiment | a | b | ε | y_o | σ | γ | β | Ω | d |
|------------------------------------|-------|------|---------------|-------|--------------------|----------|---------|------------------|-------------------------------------|
| 1 – steady symmetric | 0.62 | 7.5 | 0 | 0 | 0 | 0 | 0 | 0 | 10^{-3} |
| 1a (small Ω) | 0.62 | 7.5 | 0 | 0 | 0 | 0 | 0 | 0.3 | 10^{-3} |
| 1b (large Ω) | 0.62 | 7.5 | 0 | 0 | 0 | 0 | 0 | 1 | 10^{-3} |
| 1c (slow overturn) | 0.62 | 0.25 | 0 | 0 | 0 | 0 | 0 | 1 | 10^{-3} vs. 5×10^{-4} |
| 1d ($z_{attractor}$ vs Ω) | 0.62 | 7.5 | 0 | 0 | 0 | 0 | 0 | Sweep 0 to 10 | 10^{-3} |
| 1e (reversed flow) | -0.62 | -7.5 | 0 | 0 | 0 | 0 | 0 | 0, 0.6, 2 | 10^{-3} |
| 2 – steady asymmetric | 0.62 | 7.5 | 0.25 | -0.2 | 0 | 0 | 0 | 0 | 10^{-3} |
| 2a (small Ω) | 0.62 | 7.5 | 0.25 | -0.2 | 0 | 0 | 0 | 0.3 | 10^{-3} |
| 2b (large Ω) | 0.62 | 7.5 | 0.25 | -0.2 | 0 | 0 | 0 | 1 | 10^{-3} |
| 2c (2:1 resonance) | 0.62 | 3.8 | 0.25 | -0.2 | 0 | 0 | 0 | 0 | 10^{-3} |
| 3 - non-steady asymmetric | 0.62 | 7.5 | 0.25 | -0.2 | $\frac{2\pi}{9.1}$ | 0.2 | 1 | 0 | 10^{-3} |

728 Table 1: Dimensionless parameter values for numerical experiments. Fixed parameters in the

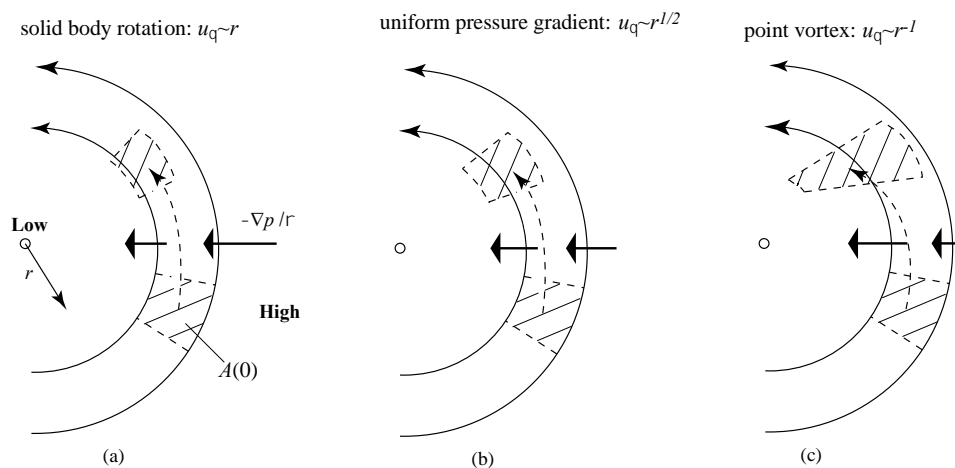
729 kinematic model (Eqs. 9a-c) are $c=0.69$, and $r_o=1/2$ in all cases. Parameters that appear in the

730 nondimensional Maxey-Riley equation (3) are also nondimensional, with $L, U, L/U$ as length,

731 velocity and time scales. Fixed parameter values based on $L=1m$ and $U=1m/s$ include $\frac{\rho_p}{\rho_f} =$

732 $0.97, R = \frac{2\rho_f}{\rho_f+2\rho_p} = 0.680, \frac{3R}{2} - 1 = .020, \tilde{g}_r = \frac{gL}{U^2} = 10.0, \tilde{\varepsilon} = \frac{2}{9} \left(\frac{d}{L}\right)^2 \frac{UL}{\nu} = 0.33,$ and $\tilde{\varepsilon} \left(\frac{3R}{2} -$

733 $1\right) = .0067.$ Note that $\bar{\Omega} = \Omega \bar{k} = \frac{\bar{\Omega}^* L}{U}.$



734

735 Figure 1. Three types of two-dimensional eddies with zero frame rotation and for which gravity
736 is imagined to be zero: solid body rotation (a), constant pressure gradient (b), and point vortex
737 (c). In each case, the cross hatched area represents a concentration of rigid particles with area
738 $A(t)$.

739

740

741

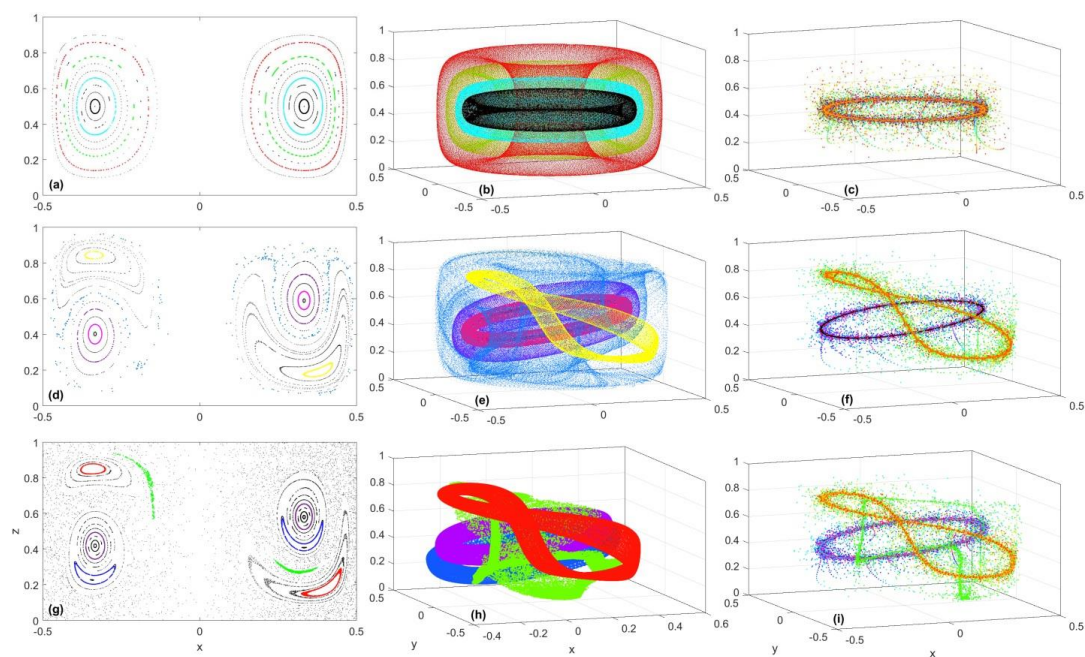
742

743

744

745

746



747

748 Figure 2. (left) Poincare section, (middle) fluid parcels trajectories in 3D, (right) buoyant particle

749 trajectories in 3D for a steady symmetric fluid flow (top row), steady asymmetric flow (middle

750 row), and non-steady, asymmetric flow. Parameter setting are listed under Experiments 1, 2 and

751 3 in Table 1. Colors in the left column of panels match the corresponding panel in the middle

752 column, but the colors in the right column indicated time after release of the particles. Note the

753 attraction of buoyant particles to a single attractor at mid-depth in panel (c), to 2 attractors in

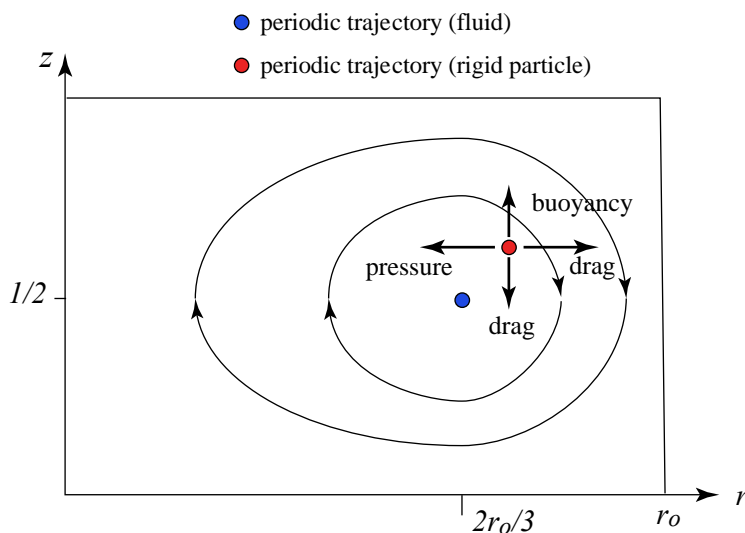
754 panel (f), and to 3 attractors in panel (i). Particles are released along a vertical line $x = 0.334$,

755 $y = 0$, $0 < z \leq 0.6$ with initial velocity equal to that of the co-located fluid parcels.

756

757

758



759

760 Figure 3. Sketch showing the position in a vertical section of the periodic orbit (red dot) of the
761 rigid particle relative to the periodic orbit (blue dot) of the fluid flow. The viewer sees one half
762 of a vertical slide through the cylinder, with the azimuthal flow directed away from the viewer
763 and the cylinder center at the left edge.

764

765

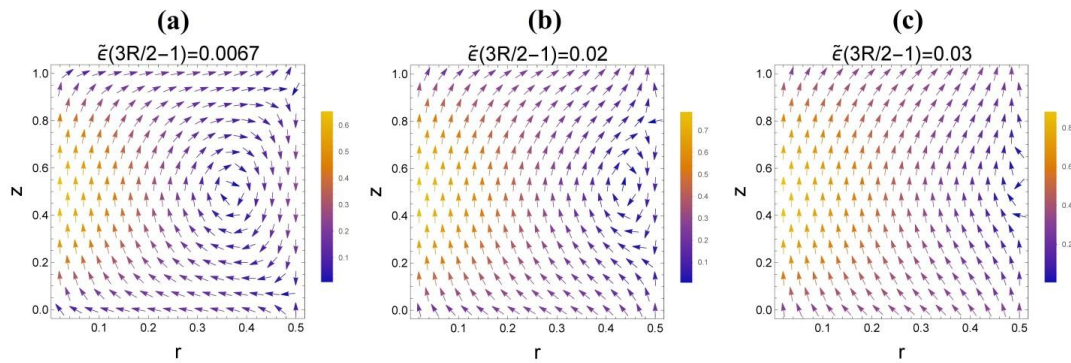
766

767

768

769

770



771

772 Figure 4. The slow-manifold radial and vertical velocity components for the rigid particles,

773 plotted in the (r, z) plane for (a) $\tilde{\epsilon} \left(\frac{3R}{2} - 1 \right) = .0067$, (b) $= .02$, and (c) $= .03$. Other parameters are

774 as listed for Experiment 1a in Table 1.

775

776

777

778

779

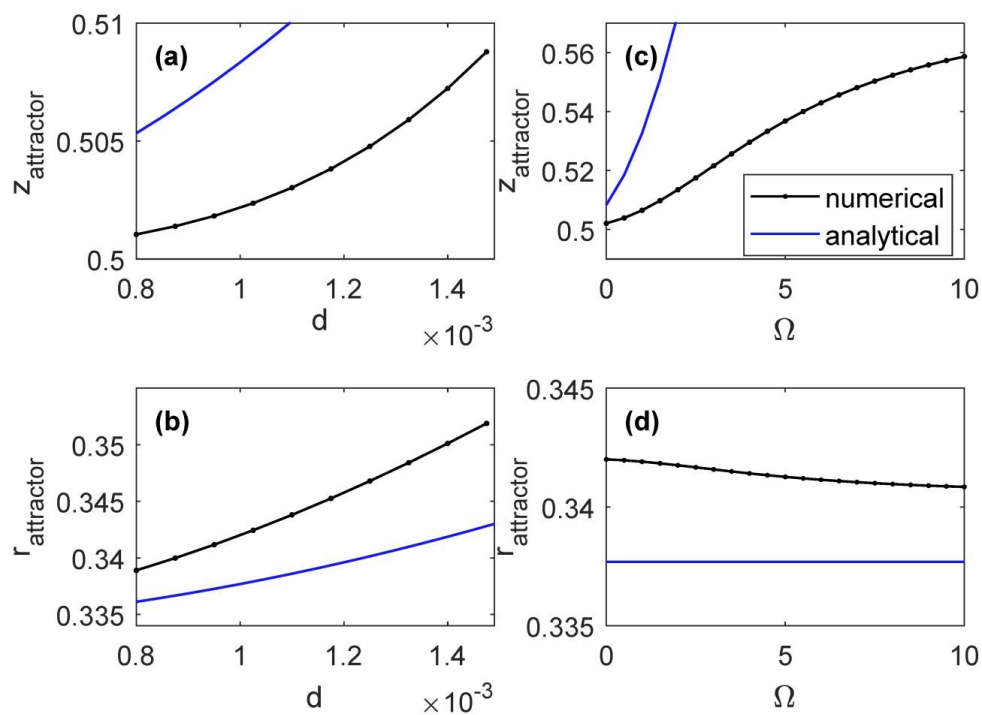
780

781

782

783

784



785

786 Figure 5. For the steady symmetric rotating cylinder flow, the coordinates of the periodic orbit
787 that acts as an attractor for buoyant particles as a function of particle diameter (a-b) and frame
788 rotation (c). Flow parameters are listed in Table 1 and correspond to Experiment 1 for (a-b) and
789 Experiment 1d for (c-d).

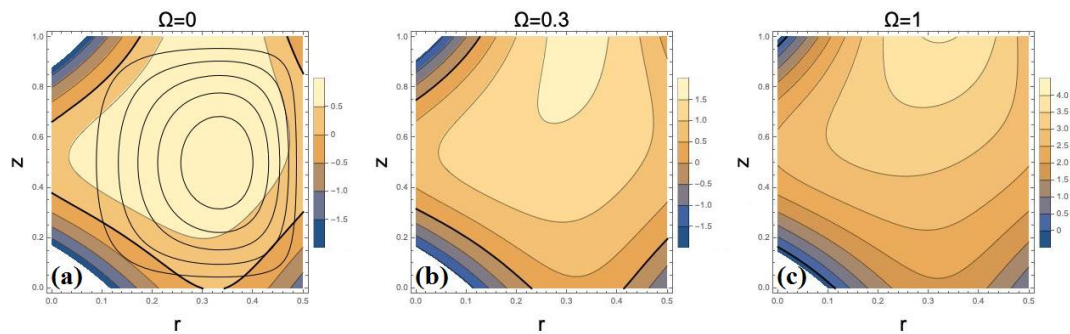
790

791

792

793

794



795

796 Figure 6. (a): The Q_a function for the steady, axisymmetric, cylinder flow with the same
797 parameter setting (see Experiment 1a) as for Figure 3a-c, and plotted in (x,z) along with the
798 streamlines of the overturning circulation. The thick rigid curve corresponds to $Q_a=0$. (b): The
799 same parameter settings, except Ω has been raised from 0 to 0.3 (Rossby number $\cong 1$) (c):
800 $\Omega=1.0$. (Rossby number $\cong 0.2$).

801

802

803

804

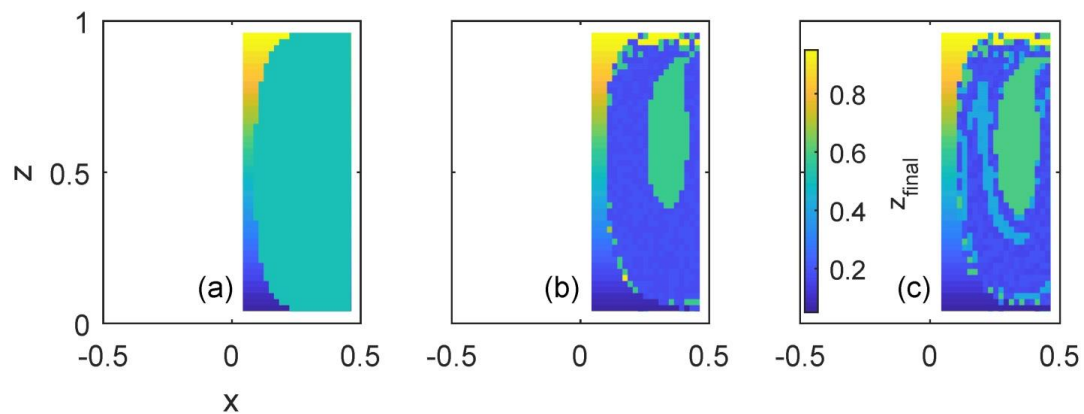
805

806

807

808

809



810

811 Figure 7. Domain of attraction for the attractors in (a) steady symmetric (Experiment 1 in Table
812 1), (b) steady asymmetric (Experiment 2 in Table 1), and (c) time-periodic asymmetric rotating
813 cylinder flow (Experiment 3 in Table 1). (These are the same 3 experiments that were used to
814 produce Fig. 2.) The color indicates the height (i.e., value of z-coordinate) of the final crossing of
815 a trajectory with the Poincare section, as a function of particle's release location. Particles
816 attracted to the same attractor thus correspond to same color.

817

818

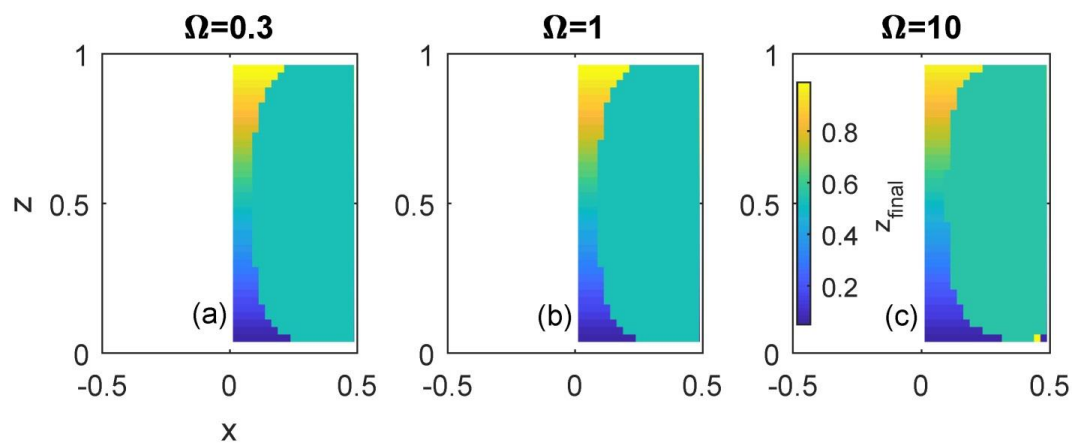
819

820

821

822

823



824

825 Figure 8. Same as in Fig. 7a but with frame rotation.

826

827

828

829

830

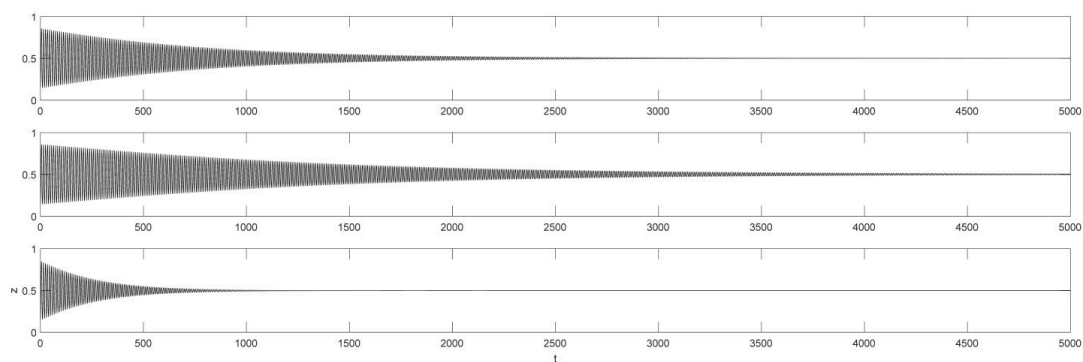
831

832

833

834

835



836

837 Figure 9. For the “reversed flow” experiment (Experiment 1e in Table 1), z-position of a sample

838 particle trajectory as function of time for 3 values of Ω : 0 (top), 0.6 (middle), and 2 (bottom).

839 Time t is in dimensionless units (but since our scaling coefficient for time is equal to 1 sec, the

840 numbers on the x-axis can also be read as dimensional time in sec.)

841

842

843

844

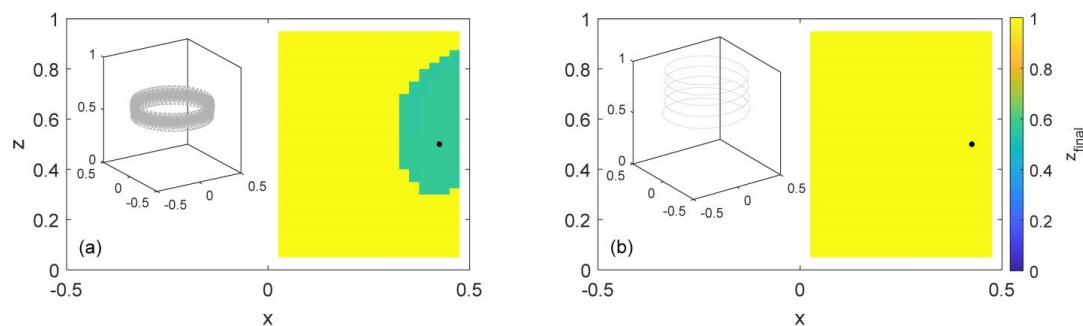
845

846

847

848

849



850

851 Figure 10. For the “slow overturn” Experiment 1c from Table 1, color indicates the final z-
852 coordinate of a particle’s trajectory at the end of integration time as a function of particle’s
853 release location for 2 values of d: (a) 5×10^{-4} and (b) 10^{-3} . Yellow corresponds to particles
854 rising up to the top, whereas green indicates the basin of attraction of the subsurface attracting
855 periodic orbit. The insets at the left side of each frame show a sample trajectory whose release
856 location is indicated by the black dot.

857

858

859

860

861

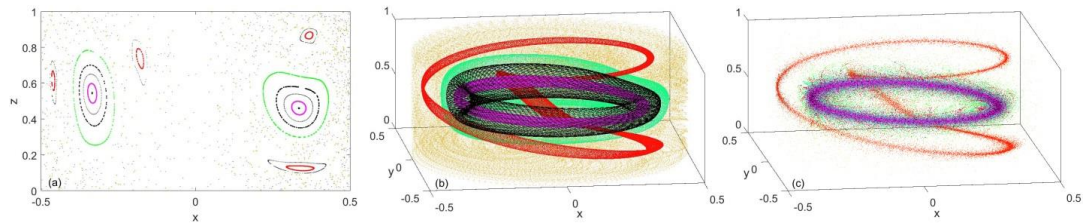
862

863

864



865



866

867 Figure 11. Same as Fig. 2(d-f) but with $b=3.8$.

868

869

870

871

872

873

874

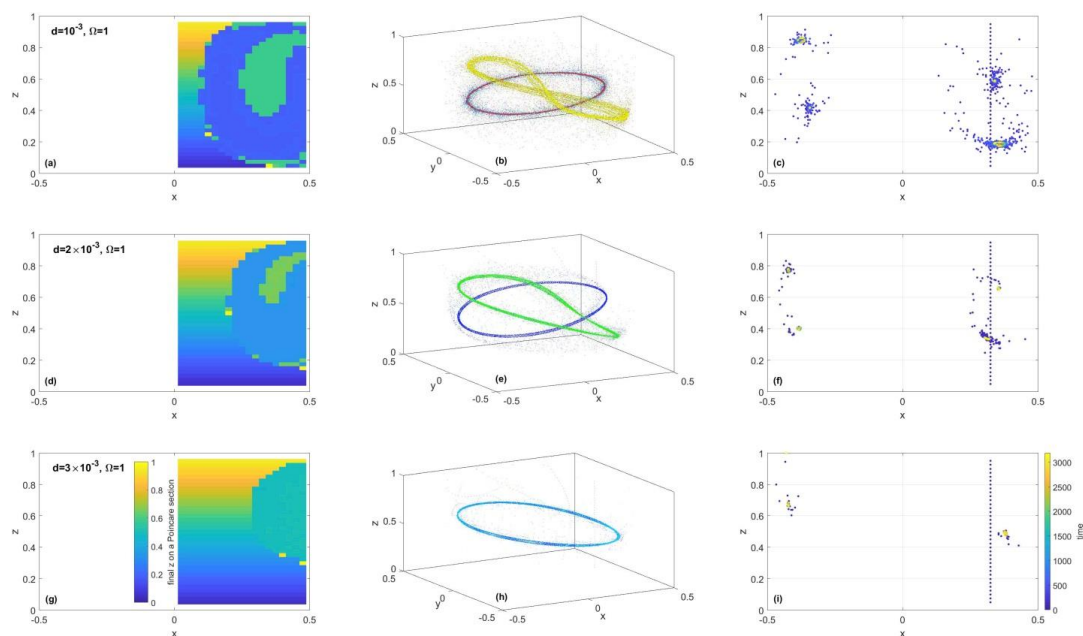
875

876

877

878

879



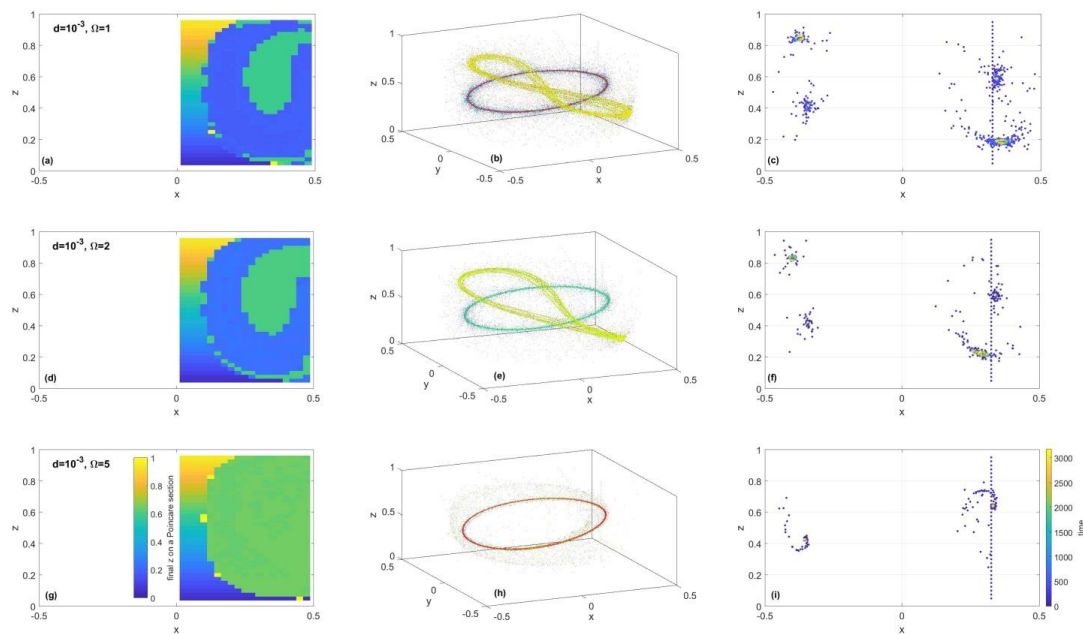
880

881 Figure 12. For the steady perturbed system (Experiment 2 in Table 1), changes in the location of
 882 the attracting periodic orbits, basins of attractions, and time of attraction as a function of particle
 883 diameter d (and thus $\tilde{\epsilon}$). (a,d,g) show z -coordinate of the last crossing of trajectory with the x - z
 884 Poincare plane as a function of release location; flat regions are basins of attraction for the 2
 885 attractors. (b,e,h) show 20 trajectories in 3d released along a vertical line at $y=0, x=0.334,$
 886 $0.05 < z < 0.95$; denser cores indicate attractors. (c,f,i) show crossing of the same select 20
 887 trajectories with the x - z Poincare plane, color coded by time; blue corresponds to release
 888 location, yellow corresponds to final positions.

889

890

891



892

893 Figure 13. For the steady perturbed system (Experiment 2 in Table 1), changes in the location of
 894 the attracting periodic orbits, basins of attractions, and time of attraction as a function of frame
 895 rotation Ω . (a,d,g) show z-coordinate of the last crossing of trajectory with the x-z Poincare plane
 896 as a function of release location; flat regions are basins of attraction for the 2 attractors. (b,e,h)
 897 show 20 select trajectories in 3d released along a vertical line at $y=0, x=0.334, 0.05 < z < 0.95$;
 898 denser cores indicate attractors. (c,f,i) show crossing of the same 20 trajectories with the x-z
 899 Poincare plane, color coded by time; blue corresponds to release location, yellow corresponds to
 900 final positions.

901

902

903